CHINESE OPTICS LETTERS

Vol. 22, No. 1 | January 2024

Toroidal dipole response in rectangular waveguide: used to generate vector beams and vector vortex beams

Hao Luo (罗 灏), Cong Chen (陈 聪), Peng Gao (高 鹏), Yue Feng (冯 越), Ziyan Ren (任紫燕), Yujia Qiao (乔昱嘉), and Hai Liu (刘 海)*

School of Information and Control Engineering, China University of Mining and Technology, Xuzhou 221116, China

*Corresponding author: lhai_hust@hotmail.com

Received June 12, 2023 | Accepted September 5, 2023 | Posted Online January 22, 2024

Toroidal multipole is a special current distribution that has many different characteristics from electric multipole and magnetic multipole distributions. Because of its special properties, the toroidal dipole is a research hotspot in the field of metamaterials and nanophotonics. However, the low scattering of the toroidal dipole moment makes its excitation a challenging task. At present, there are relatively few studies on its specific engineering applications. In this paper, by slotting in the rectangular cavity, the excitation of an equivalent toroidal dipole is successfully achieved over a wide frequency range of 53–58 GHz. Results indicate that under the action of the toroidal dipole, the TE_{10} mode electromagnetic waves transmitted in the rectangular waveguide are converted into vector beams and are radiated outwards. Further adjusting the spatial distribution of the magnetic dipoles in the toroidal dipoles yields results that indicate that the resonance mode in the slot is still dominated by the magnetic toroidal dipole moment, and the electromagnetic waves radiating outward are vortex beams carrying vector polarization. The scattered energy of each dipole moment inside the antenna is calculated. This calculation verifies that the mass of the vector beam and vector vortex beam is closely related to the toroidal dipole supported by this antenna. The proposed structure can be applied to explorations in vortex filtering, in photon entanglement, and in the photonic spin Hall effect.

Keywords: toroidal dipole; vector beams; vector vortex beams.
DOI: 10.3788/COL202422.011601

1. Introduction

Toroidal multipole is a peculiar electromagnetic excitation, its closed toroidal current cannot be directly represented by an electric/magnetic multipole. Toroidal multipole was originally first proposed by Zel'dovich to explain parity violation in weak interactions[1]. In fact, in some solid systems such as ferroelectric systems, macromolecules, and molecular magnets, the role of the toroidal dipole moment cannot be ignored[2–4]. In condensed matter physics, the toroidal dipole moment has also been responsible for some unusual phenomena[5–7]. Due to its special properties, toroidal multipole is currently a research hotspot in the field of nanophotonics and metamaterials.

Although dynamic toroidal dipole moments can radiate electromagnetic waves to the far field just like electric/magnetic dipole moments, it is not included in the standard multipole expansion and is thus often omitted from considerations in classical electrodynamics[8–11]. The far-field radiation produced by the toroidal dipole is completely consistent with the electric dipole moment, and the destructive interference between them will produce a special nonradiative state called the anapole mode[12,13]. It is still uncertain whether this non-radiative mode can produce the Aharonov–Bohm effect and further experimental proof is needed.

Due to the low scattering energy of the toroidal dipole moment, its excitation has always been a challenging task. The toroidal multipole performance is usually masked by the electric/magnetic multipole. In recent years, with the development of metamaterials, significant progress has been made in the excitation and research of the electric/magnetic toroidal dipole. Since Zheludev achieved the excitation of magnetic toroidal dipole using multiple metal rings in 2010[14], researchers have realized the excitation of electric toroidal dipole and magnetic toroidal dipole by using dielectric cylinders, metal arms, metal rings, and other structures. However, most of the current research on the toroidal dipole is focused on its interaction with other modes, and the application of the toroidal dipole itself in engineering is seldom studied.

Different from the traditional plane electromagnetic wave, the electromagnetic wave carrying orbital angular momentum (OAM) has a spiral phase distribution, so it is called a vortex beam. Using the orthogonal characteristics of the vortex beam

OAM modes, the mode division of the OAM can be realized to improve the transmission rate of wireless communication[15,16]. The OAM carried by the vortex beam can be transferred to particles, which can be adopted to realize the operation of small particles[17,18]. In addition, the rotating Doppler effect produced by the vortex beam can be used to measure the rotation speed of the object and the flow velocity of the fluid[19–21].

Compared with the traditional vector beam and the vortex beam, the vector vortex beam is a new type of structured optical field with a helical phase and cross-sectional anisotropic polarization distribution, which has been proposed and explored in various applications, such as vector optical vortex filtering[22], particle acceleration[23], photon entanglement[24], and photon spin Hall effect[25,26]. Driven by these applications, researchers have proposed many means to generate vector vortex beams, including using a spatial light modulator[27], a laser resonator configuration[28,29], a metasurface[30], and a vector beam combined with spiral phase plate[31]. However, most of these methods face challenges of having a low damage threshold and a lower conversion efficiency, and require a large volume to manipulate the phase of the electromagnetic waves, making it difficult to reduce the overall volume.

In this paper, we first investigated the effect of toroidal dipole moments in angularly distributed dipoles. Results showed that when the magnetic toroidal dipole moment dominates, the electromagnetic waves radiating outward carry radial polarization. Furthermore, by offsetting the spatial position of each dipole in the toroidal dipole, the vector vortex electromagnetic wave is successfully generated with little effect on the vector polarization part. Results indicate that the OAM mode vector vortex beam with $l = 1$ is generated in the range of 55 GHz to 57 GHz. The designed resonant cavity structure is relatively simple and easy to manufacture, which can easily realize the generation of the vortex beam without a complicated phase control structure. The method of vector vortex beam generation using the toroidal dipole is universal and can be extended to high frequencies in the future.

2. Theoretical Analysis

The main challenge of exciting the toroidal dipole moment is to find the structure that supports the dynamic annular electric/magnetic field on the surface. In the field of metamaterials, electric dipole $\vec{p}$, magnetic dipole $\vec{M}$, electric quadrupole $\vec{Q}_e$, magnetic quadrupole $\vec{Q}_m$, electric toroidal dipole moment $\vec{G}$, and magnetic toroidal dipole moment $\vec{T}$ can be expressed as

$$\vec{p} = \frac{1}{i\omega}\int \vec{j}\,\mathrm{d}^3 r, \tag{1}$$

$$\vec{G} = \frac{1}{2}\int (\vec{r}\times\vec{p})\,\mathrm{d}^3 r, \tag{2}$$

$$\vec{M} = \frac{1}{2c}\int (\vec{r}\times\vec{j})\,\mathrm{d}^3 r, \tag{3}$$

$$\vec{T} = \frac{1}{10c}\int [(\vec{r}\cdot\vec{j})\vec{r} - 2r^2\vec{j}]\,\mathrm{d}^3 r, \tag{4}$$

$$\vec{Q}^{(e)}_{\alpha,\beta} = \frac{1}{i2\omega}\int \left[\vec{r}_\alpha \vec{j}_\beta + \vec{r}_\beta \vec{j}_\alpha - \frac{2}{3}(\vec{r}\cdot\vec{j})\delta_{\alpha,\beta}\right]\mathrm{d}^3 r, \tag{5}$$

$$\vec{Q}^{(m)}_{\alpha,\beta} = \frac{1}{3c}\int [(\vec{r}\times\vec{j})_\alpha \vec{r}_\beta + (\vec{r}\times\vec{j})_\beta \vec{r}_\alpha]\,\mathrm{d}^3 r, \tag{6}$$

where $\vec{j}$ is the current density, and c is the speed of light in a vacuum. The total electromagnetic scattering energy can be expressed as

$$I = \frac{2\omega^4}{3c^3}|\vec{p}|^2 + \frac{2\omega^4}{3c^3}|\vec{M}|^2 + \frac{2\omega^6}{3c^5}|\vec{G}|^2 + \frac{2\omega^6}{3c^5}|\vec{T}|^2 + \frac{\omega^6}{5c^5}\sum |\vec{Q}^{(e)}_{\alpha,\beta}|^2 + \frac{\omega^6}{20c^5}\sum |\vec{Q}^{(m)}_{\alpha,\beta}|^2 + o(\omega). \tag{7}$$

This method can quickly confirm which dipole moment dominates the resonance peak, thereby linking the surface current with the distribution mode of the far field.

The circularly polarized basis vector of the Poincaré sphere can be generalized to the circularly polarized vortex basis vector with opposite topological charges. The left-handed and right-handed circular polarization vortex basis vectors with topological charges of n and m can be expressed as[32]

$$L_n = e^{in\varphi}(\boldsymbol{e}_x - i\boldsymbol{e}_y)/\sqrt{2}, \tag{8}$$

$$R_m = e^{im\varphi}(\boldsymbol{e}_x + i\boldsymbol{e}_y)/\sqrt{2}. \tag{9}$$

In the paraxial approximation, the generalized vector vortex beam can be represented as

$$U_m = U^n_L L_n + U^m_R R_m, \tag{10}$$

where U^n_L and U^m_R are the plural amplitudes on the basis vectors of two circular polarization vortices, respectively. By extracting a common spiral phase factor of $e^{i(n+m)\varphi/2}$, the formula above will be converted to

$$U_m = \frac{1}{\sqrt{2}} e^{\frac{i(n+m)\varphi}{2}}\left[U^n_L e^{\frac{i(n-m)\varphi}{2}}(\boldsymbol{e}_x - i\boldsymbol{e}_y) + U^m_R e^{\frac{i(m-n)\varphi}{2}}(\boldsymbol{e}_x + i\boldsymbol{e}_y)\right]. \tag{11}$$

Compare Eq. (8) with the general form of the vector beam obtained in reference[31]

$$|\psi\rangle = \frac{1}{\sqrt{2}}\left[\cos\frac{\vartheta'}{2}(\boldsymbol{e}_x + i\boldsymbol{e}_y)e^{-i\sigma\varphi} + \sin\frac{\vartheta'}{2}(\boldsymbol{e}_x - i\boldsymbol{e}_y)e^{i\sigma\varphi}\right]. \tag{12}$$

Clearly, this expression is equivalent to the expression in the parentheses in Eq. (8), which only differs by a spiral phase factor of $\exp[i(n+m)\varphi/2]$. To generate a vector vortex beam, some researchers have combined the vector beam with a spiral phase

plate to obtain the helical phase factor of the vector beam. In our work, we have rearranged the radiation slots for the generation of the vector beams to enable the generation of the vector vortex beams without compromising the quality of the vector beam. This method does not require a helical phase plate or other phase adjustment structures and therefore significantly reduces the overall size.

3. Theoretical Model and Parameter Optimization

The structure designed in this article is illustrated in Fig. 1. All structures are composed of metal and are set as PEC in the simulation. The parameters of the resonant cavity structural units are as follows: $h_1 = 2.3$ mm, $h_2 = 3.9$ mm, $h_3 = 0.5$ mm, $h_4 = 1$ mm, $h_5 = 4$ mm, $d_1 = 9.4$ mm, $d_2 = 7.6$ mm, $w_1 = 6.5$ mm, offset = 1.3 mm, $\text{feed}_x = 2.5$ mm, $\text{feed}_y = 0.4$ mm, $\text{slot}_x = 3$ mm, $\text{slot}_y = 0.4$ mm, $l_1 = 0.8$ mm, $l_2 = 0.4$ mm. Due to the vector vortex beam having the characteristics of outward divergence, a circular horn is designed at the top layer to adjust its beam width and to better observe the characteristics of the vector vortex beam.

4. Results and Discussions

Researchers have used radially polarized light to excite magnetic toroidal dipole resonance[33] because of the similar magnetic field distribution between the radially polarized light and the TE_{10} mode in rectangular waveguides. This paper achieves the excitation of toroidal dipoles by slotting on the rectangular waveguide. An equivalent magnetic dipole can be achieved by

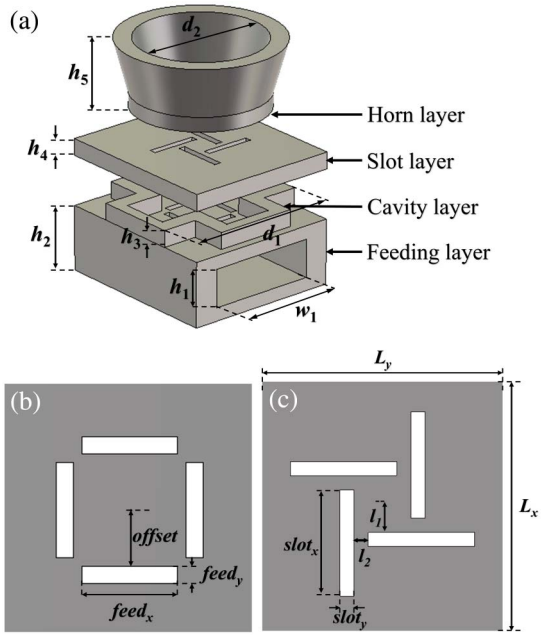

Fig. 1. Resonant cavity design. (a) 3D view, (b) top view of the feeding layer, and (c) top view of the slot layer.

opening a slot in the waveguide wall. In order to excite the resonance of the magnetic toroidal dipole, four slots are cut out on the rectangular waveguide and arranged along the annular direction. The S-parameter response and far-field radiation diagram with only the lower slot structure are simulated, as illustrated in Fig. 2. Clearly, a sharp formant appears at 56.9 GHz. The far-field radiation pattern at 56.9 GHz is a typical hollow beam, which confirms that the electromagnetic moment oscillates along the z-axis. The pattern in the x-direction is slightly asymmetric because the upper and lower magnetic dipole moments are slightly different. To confirm the resonance mode, the response distributions of the electric field and magnetic field at 56.9 GHz are simulated in Figs. 2(c)–2(e). The Z-component magnetic field is twisted into an annulus, which causes the magnetic dipole to connect the head-to-tail. There is a phase singularity in the center of the four slots where the field strength is close to zero.

The scattering energy of each multipolar moment supported in the slot is calculated as shown in Fig. 2(b). It can be seen that in the wide band range of 52 GHz to 60 GHz, the magnetic toroidal dipole moment $\vec{T}$ has always occupied the dominant position. Because the magnetic dipole moment supported by each slot is distributed along the annulus, its scattering energy is greatly suppressed, and the overall scattering energy is close to the electric dipole moment.

Figure 3 shows the amplitude and phase distribution of the far-field magnetic field of the annular slot. The outgoing magnetic field is deflected into a toroidal, which is also one of the important characteristics of the magnetic toroidal dipole. By analyzing the emitted electric and magnetic fields, it can be seen that the emitted electromagnetic waves carry radial polarization.

The effects of different slot combinations on the S-parameters were simulated, as Fig. 4(a) shows. It is worth mentioning that the radiation slots on the left and right sides are not in accordance with the maximum points of the TE_{10} mode. Only the presence of the slots on both sides can hardly radiate electromagnetic waves to the outside. But after adding the slot along the x-direction, the radiation efficiency of the slot on both sides increases and remains almost the same as the upper and lower slots. This simulated the impact of each magnetic dipole spacing on the overall radiation mode, as shown in Figs. 4(b) and 4(c). As the spacing between each magnetic dipole increases, the radiation efficiency of the designed antenna also goes up, but its far-field mode quickly shifts from hollow beams to other modes. This is mainly due to the increase in slot spacing, which makes it closer to the extreme point of the TE_{10} mode, but correspondingly, its resonance mode will be converted into a magnetic dipole resonance. The far field of the vector beam is a hollow beam, so when the value of the offset is increased the resulting beam will not carry vector polarization.

The space/phase distribution of each magnetic dipole in the toroidal dipole is further adjusted to make it carry spiral phase factor and finally realize the generation of the vector vortex beam. Moving the slots of each dipole in the toroidal dipole directly onto a rectangular waveguide will result in different radiation efficiencies of each dipole. Therefore, we adopt a

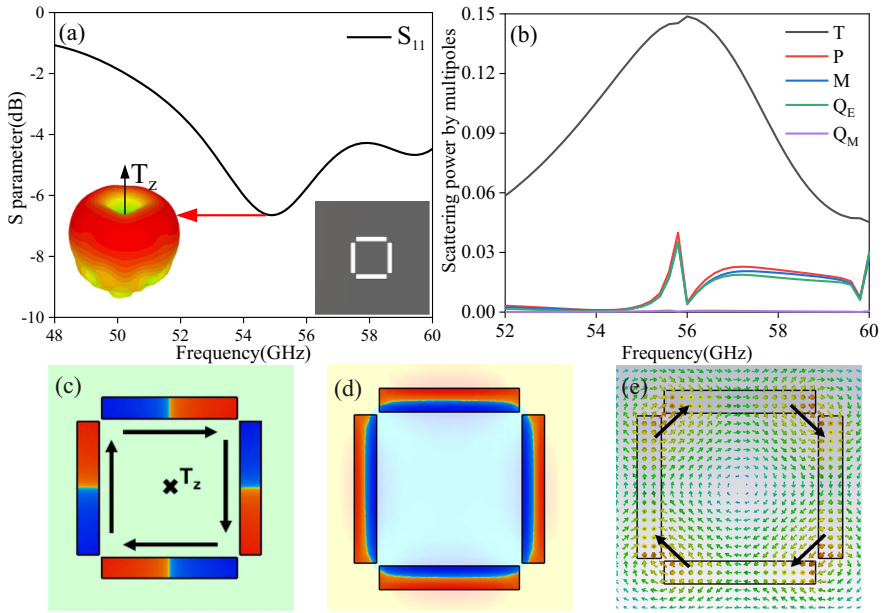

Fig. 2. (a) The S-parameter response and far-field pattern. (b) The calculation of the multipole scattering energy of each multipole moment. (c) The *Z*-component magnetic field. (d) The *Z*-component electric field. (e) The slot surface magnetic field.

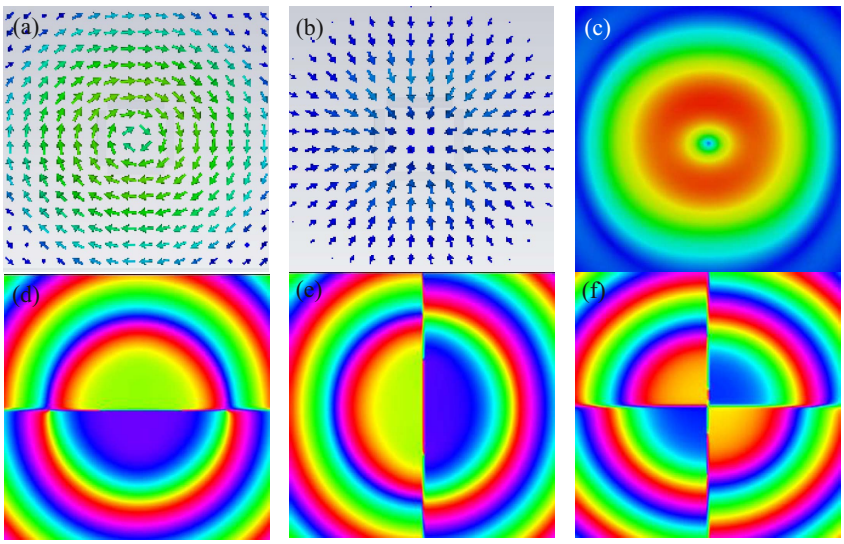

Fig. 3. (a) The magnetic field distribution of the outgoing electromagnetic wave. (b) The electric field distribution of the outgoing electromagnetic wave. (c) The magnetic field amplitude of the outgoing electromagnetic wave. (d)–(f) The Phase distribution of H_x, H_y, and H_z.

back-cavity structure with stable modes to complete the design. In order to adjust the spatial distribution of each dipole in the toroidal dipole, a cross-shaped metal back cavity is designed on the basis of the original. When there is no metal short-circuit wall, the back cavity can be regarded as a four-way equal power divider. The simulation results of the structure are shown in Figs. 5(a)–5(c).

The slot in the metal plate can radiate electromagnetic energy, which is mainly because it truncates the continuous current in the metal plate so that the radiation slot generates an equivalent magnetic dipole. In order to realize the generation of the vector vortex beam, we have modified the rectangular groove of the previous annular distribution and set four rectangular slots with the same offset on the top of the metal back cavity. The electromagnetic response of the resonant cavity is shown in Fig. 6(a). An obvious formant appears at 56.1 GHz, and at this time, the far-field radiation pattern is still a hollow beam. To further confirm the resonance mode in the radiation slot, the surface current distribution of the top metal plane and the electromagnetic energy distribution in the radiation gap were analyzed in

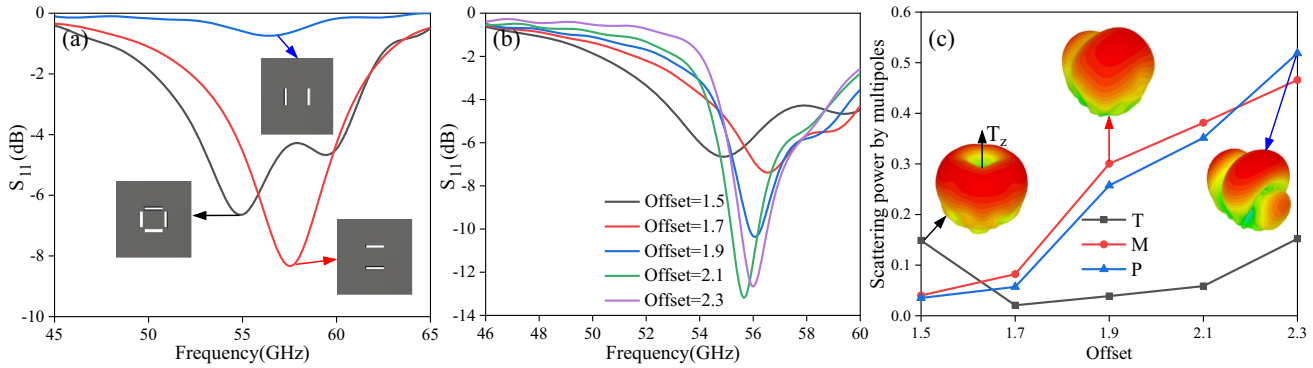

Fig. 4. (a) The S-parameter response for the different combinations of the radiation slots. (b) The effect of offset on the S-parameters. (c) The far-field radiation when different dipole moments dominate.

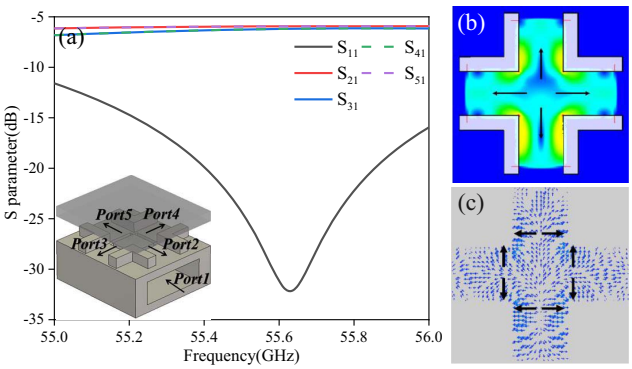

Fig. 5. (a) S-parameter response without the top radiation slot and metal short-circuit wall. (b) Magnetic field distribution in the cavity layer. (c) Surface current distribution of the top metal.

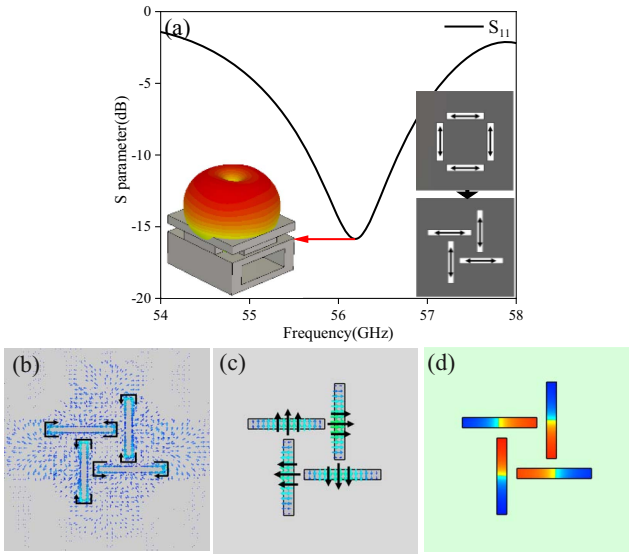

Fig. 6. (a) The S-parameter response and far-field pattern of the designed structure. (b) The surface current distribution of the top metal plane. (c) The electric field distribution in the radiation slot. (d) The *Z*-component magnetic field at 56.1 GHz.

Figs. 6(b) and 6(c). The generated magnetic dipole is distributed outward along the center.

The phase distribution of the electric field emitted at each frequency is analyzed, as shown in Fig. 7. The outgoing beam has a spiral phase distribution in the frequency range of 53 GHz to 57 GHz, and the central phase singularity is visible. At this time, the outgoing beam is a high-quality vortex beam that carries an OAM mode with $l = 1$. The quality of the vector vortex beam has significantly decreased at 58 GHz. We calculated the multipole scattering energy of the radiation slot at this time, as shown in Fig. 8. It is clear that the scattering energy of the toroidal dipole decreases rapidly with increasing frequency, and its scattering energy is surpassed by other dipoles around 58 GHz, which ultimately leads to a decrease in the mass of the vector vortex beam. In summary, it can be concluded that the intensity of the scattering energy of the toroidal dipole has a significant impact on the quality of the vortex beam in the designed antenna system.

To confirm the polarization state carried by the outward radiation vortex beam, the generated vortex beam is incident on different polarizers. As shown in Fig. 9, the field distribution radiating outward at this time is consistent with the previously

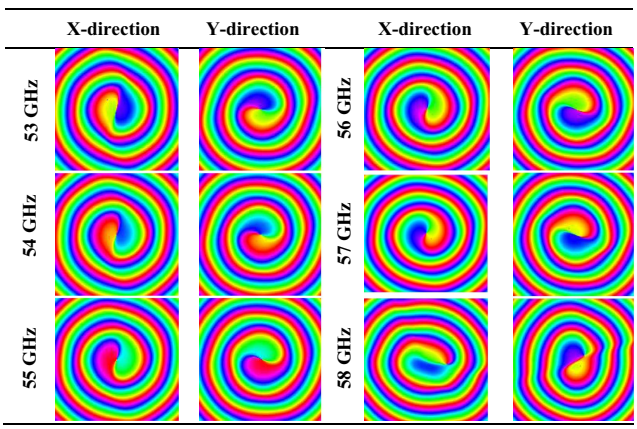

Fig. 7. Far-field phase distribution of the designed resonator in the range of 53 GHz to 58 GHz.

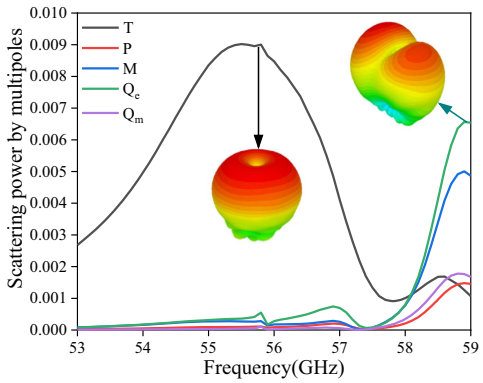

Fig. 8. Calculation results of the multipole scattering energy in a radiation slot.

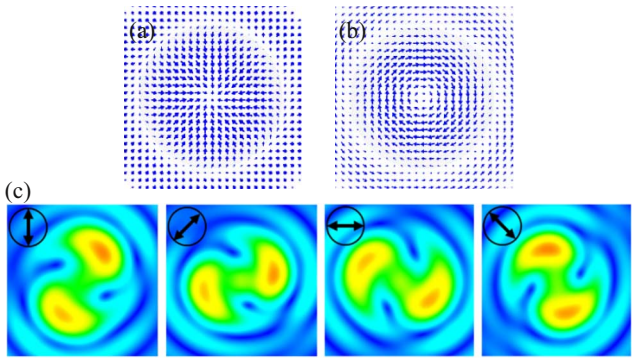

Fig. 9. (a) The electric field distribution. (b) The magnetic field distribution. (c) The intensity distribution of the vector vortex beam passing through different polarizers. (Only the polarization state in the direction of the arrow is allowed to pass through.)

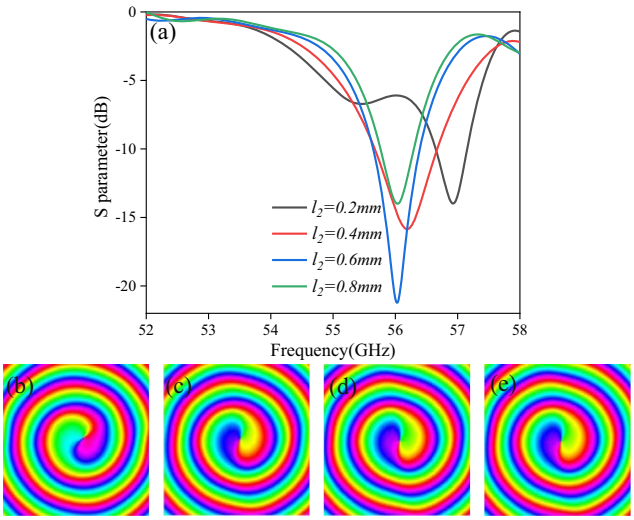

Fig. 10. (a) The influence of l_2 on the S-parameter. (b)–(e) The phase distribution of the emitted electric field at the peak under different offsets.

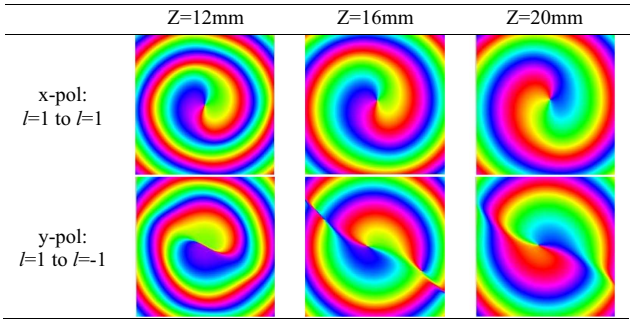

Fig. 11. OAM pattern variation of the *x*-polarized and *y*-polarized electric fields with propagation distance (*Z* is the distance between the observation plane and the antenna base).

excited vector beam, but the phase distribution of the two is completely different. When the polarizer is rotated, the electric field intensity distribution shows a typical S-type pattern, and its rotation direction is the same as that of the polarizer. The intensity is close in all directions. At this time, the vortex beam radiating outward is not the traditional scalar vortex beam with linear/circular polarization. The field intensity distribution after passing through the polarizer is consistent with the classical vector vortex beam.

The influence of the top radiation slot offset on the S-parameter and the quality of the generated vortex beam is analyzed, as shown in Fig. 10. With the increase of the offset, the intensity of the formant experienced a process from strong to weak. When the offset is set as 0.6 mm, the formant peak value reaches −22 dB, but the −10 dB bandwidth also decreases significantly. Therefore, $l_2 = 0.4$ mm is selected as the parameter to design the resonant cavity. In addition, the phase distribution of the outgoing electric field in the *x*-direction with different offsets is simulated. The offset has little effect on the overall vortex phase distribution, which provides convenience for machining.

Different from traditional scalar vortex beams, in some cases, vector vortex beams may exhibit changes in the OAM mode along the propagation direction[34]. The vector vortex beams antenna designed in this paper also presents a similar situation. When l_2 is set as 0.6 mm, a special vortex beam appears at 56.5 GHz. At this time, the orbital angular momentum mode of the *x*-polarized electric field remains constant with the direction of propagation and always maintains the mode $l = 1$. In contrast, the *y*-polarized electric field shifts from the $l = 1$ mode to the $l = -1$ mode as the propagation distance increases.

Finally, the proposed method is compared with existing antenna arrays or metasurfaces that generate vortex beams. The contrast structure is mainly the traditional scalar vortex beam generation method. Compared with the traditional metasurface array and antenna array, the proposed method does not require phase control structure and complex feeding networks, and the vector vortex beam can be generated by using only one resonator element. Therefore, the overall size of the resonator is greatly reduced.

Table 1. Comparison with Other Methods for Generating Vortex Beams.

Reference	Method	Size ($L \times W \times H$)	Polarization	Number of elements
[34]	Ring patch antenna	$1.67\lambda \times 2\lambda \times$ not mentioned	Not mentioned	1×1
[35]	Metasurface antenna array	$1.98\lambda \times 1.98\lambda \times 0.07\lambda$	CP	2×2
[36]	Metasurface array	$2.38\lambda \times 2.38\lambda \times 0.069\lambda$	LP	2×2
[37]	Spoof-plasmon ring resonators	$> 2.77\lambda \times 2.77\lambda \times$ not mentioned	Vector	1×1
This work	Toroidal dipole	$1.75\lambda \times 1.75\lambda \times 1.9\lambda$	Vector	1×1

5. Conclusion

In this paper, an annular slot is designed to excite the magnetic toroidal dipole, and it is used as the feeding slot. A cross-shaped back cavity and four rectangular slots with the same offset are designed to excite the vector vortex beams. Using a multipole scattering energy method to relate surface currents with far fields, the calculations show that the intensity of the scattering energy of the toroidal dipole in this antenna system is closely related to the mass of the vector beam and vector vortex beam. The analysis of the emitted electric field and magnetic field indicates that TE_{10} mode in the rectangular waveguide is converted into a vector vortex beam. The designed structure has an S-parameter of less than −10 dB in the range of 55.6 GHz to 56.7 GHz. All radiating slots are fed by the same back cavity, thus greatly reducing the overall size. The overall size of the designed antenna is only $1.75\lambda \times 1.75\lambda \times 1.9\lambda$ (including the horn on top). It can generate vector vortex beams quickly without a complex phase shifter or phase regulation. The method of generating a vector vortex beam using a single toroidal dipole is universal and could be extended to the high frequency band in the future.

Acknowledgements

This research was supported by the National Key R&D Program of China (No. 2021YFC290202), the National Natural Science Foundation of China (No. 51874301), and the Primary Research & Development Plan of Xuzhou City (No. KC20162).

References

1. I. Zel'Dovich, "Electromagnetic interaction with parity violation," Sov. J. Exp. Theor. Phys. **6**, 1184 (1958).
2. M. Kläui, C. A. F. Vaz, L. Lopez-Diaz, *et al.*, "Vortex formation in narrow ferromagnetic rings," J. Phys. Condens. Matter **15**, R985 (2003).
3. I. I. Naumov, L. Bellaiche, H. Fu, *et al.*, "Unusual phase transitions in ferroelectric nanodisks and nanorods," Nature **432**, 737 (2004).
4. Y. V. Kopaev, "Toroidal ordering in crystals," Phys. Usp. **52**, 1111 (2009).
5. B. B. Van Aken, J.-P. Rivera, H. Schmid, *et al.*, "Observation of ferrotoroidic domains," Nature **449**, 702 (2007).
6. J. Li, X.-X. Xin, J. Shao, *et al.*, "From non- to super-radiating manipulation of a dipolar emitter coupled to a toroidal metastructure," Opt. Express **23**, 29384 (2015).
7. S.-Q. Li and K. B. Crozier, "Origin of the anapole condition as revealed by a simple expansion beyond the toroidal multipole," Phys. Rev. B **97**, 245423 (2018).
8. Z.-G. Dong, P. Ni, J. Zhu, *et al.*, "Toroidal dipole response in a multifold double-ring metamaterial," Opt. Express **20**, 13065 (2012).
9. M. Gupta, V. Savinov, N. Xu, *et al.*, "Sharp toroidal resonances in planar terahertz metasurfaces," Adv. Mater. **28**, 8206 (2016).
10. Y. Fan, Z. Wei, H. Li, *et al.*, "Low-loss and high-Q planar metamaterial with toroidal moment," Phys. Rev. B **87**, 115417 (2013).
11. Z. Liu, S. Du, A. Cui, *et al.*, "High-quality-factor mid-infrared toroidal excitation in folded 3D metamaterials," Adv. Mater. **29**, 1606298 (2017).
12. A. Bhattacharya, R. Sarkar, and G. Kumar, "Toroidal electromagnetically induced transparency based meta-surfaces and its applications," iScience **25**, 103708 (2022).
13. V. Savinov, V. A. Fedotov, A. V. Rogacheva, *et al.*, "Non-radiating excitations, vector potential waves and toroidal metamaterials," in *International Quantum Electronics Conference* (2013), paper II_P_14.
14. T. Kaelberer, V. A. Fedotov, N. Papasimakis, *et al.*, "Toroidal dipolar response in a metamaterial," Science **330**, 1510 (2010).
15. G. Gibson, J. Courtial, M. J. Padgett, *et al.*, "Free-space information transfer using light beams carrying orbital angular momentum," Opt. Express **12**, 5448 (2004).
16. F. Tamburini, E. Mari, A. Sponselli, *et al.*, "Encoding many channels on the same frequency through radio vorticity: first experimental test," New J. Phys. **14**, 033001 (2012).
17. Z. Xiang, Z. Shen, and Y. Shen, "Quasi-perfect vortices generated by Pancharatnam–Berry phase metasurfaces for optical spanners and OAM communication," Sci. Rep. **12**, 1053 (2022).
18. N. B. Simpson, K. Dholakia, L. Allen, *et al.*, "Mechanical equivalence of spin and orbital angular momentum of light: an optical spanner," in *Optical Angular Momentum*, L. Allen, S. M. Barnett, and M. J. Padgett, eds. (CRC Press, 2016). p. 207
19. G. Li, T. Zentgraf, and S. Zhang, "Rotational Doppler effect in nonlinear optics," Nat. Phys. **12**, 736 (2016).
20. A. Belmonte, C. Rosales-Guzmán, and J. P. Torres, "Measurement of flow vorticity with helical beams of light," Optica **2**, 1002 (2015).
21. B. Liu, H. Chu, H. Giddens, *et al.*, "Experimental observation of linear and rotational Doppler shifts from several designer surfaces," Sci. Rep. **9**, 8971 (2019).
22. B. Zhang, Z. Chen, H. Sun, *et al.*, "Vectorial optical vortex filtering for edge enhancement," J. Opt. **18**, 035703 (2016).
23. Y. Liu, D. Cline, and P. He, "Vacuum laser acceleration using a radially polarized CO_2 laser beam," Nucl. Instrum. Methods Phys. Res. Sect. A **424**, 296 (1999).
24. J. Tang, Y. Ming, Z. X. Chen, *et al.*, "Entanglement of photons with complex spatial structure in Hermite-Laguerre-Gaussian modes," Phys. Rev. A **94**, 012313 (2016).
25. P. Li, Y. Zhang, S. Liu, *et al.*, "Manipulating the photonic spin Hall effect of fan-shaped cylindrical vector beams," Front. Opt. **40**, 4444 (2015).
26. Y. Liu, Y. Ke, H. Luo, *et al.*, "Photonic spin Hall effect in metasurfaces: a brief review," Nanophotonics **6**, 51 (2017).
27. H. Chen, J. Hao, B.-F. Zhang, *et al.*, "Generation of vector beam with space-variant distribution of both polarization and phase," Opt. Lett. **36**, 3179 (2011).

28. R. Oron, S. Blit, N. Davidson, *et al.*, "The formation of laser beams with pure azimuthal or radial polarization," Appl. Phys. Lett. **77**, 3322 (2000).
29. X. Lin, Q. Feng, Y. Zhu, *et al.*, "Diode-pumped wavelength-switchable visible pr3+:YLF laser and vortex laser around 670 nm," Opto-Electron. Adv. **4**, 210006 (2021).
30. H. Ahmed, H. Kim, Y. Zhang, *et al.*, "Optical metasurfaces for generating and manipulating optical vortex beams," Nanophotonics **11**, 941 (2022).
31. H. Zhang, L. Yao, Y. Pang, *et al.*, "Flexible and high-efficiency generation of arbitrary vector vortex beams on hybrid-order Poincaré sphere," Chin. Opt. Lett. **16**, 092601 (2018).
32. Q. Zhan, "Focusing properties of circularly polarized vortex beam," in Front. Opt. **31**, 867 (2005).
33. Y. Bao, X. Zhu, and Z. Fang, "Plasmonic toroidal dipolar response under radially polarized excitation," Sci. Rep. **5**, 1 (2015).
34. W. Li, J. Zhu, Y. Liu, *et al.*, "Realization of third-order OAM mode using ring patch antenna," IEEE Trans. Antennas Propag. **68**, 7607 (2020).
35. H. Huang and Z. Zhang, "A single fed wideband mode-reconfigurable OAM metasurface CP antenna array with simple feeding scheme," Int. J. RF Microw. Comput.-Aided Eng. **31**, e22499 (2021).
36. J. Wu, Z. Zhang, X. Ren, *et al.*, "A broadband electronically mode-reconfigurable orbital angular momentum metasurface antenna," IEEE Antennas Wireless Propag. Lett. **18**, 1482 (2019).
37. Z. Liao, J. N. Zhou, G. Q. Luo, *et al.*, "Microwave-vortex-beam generation based on spoof-plasmon ring resonators," Phys. Rev. Appl. **13**, 054013 (2020).